Volume 8 | Number 9 | September 2017 | Pages 5807–6694

Chemical Science

rsc.li/chemical-science

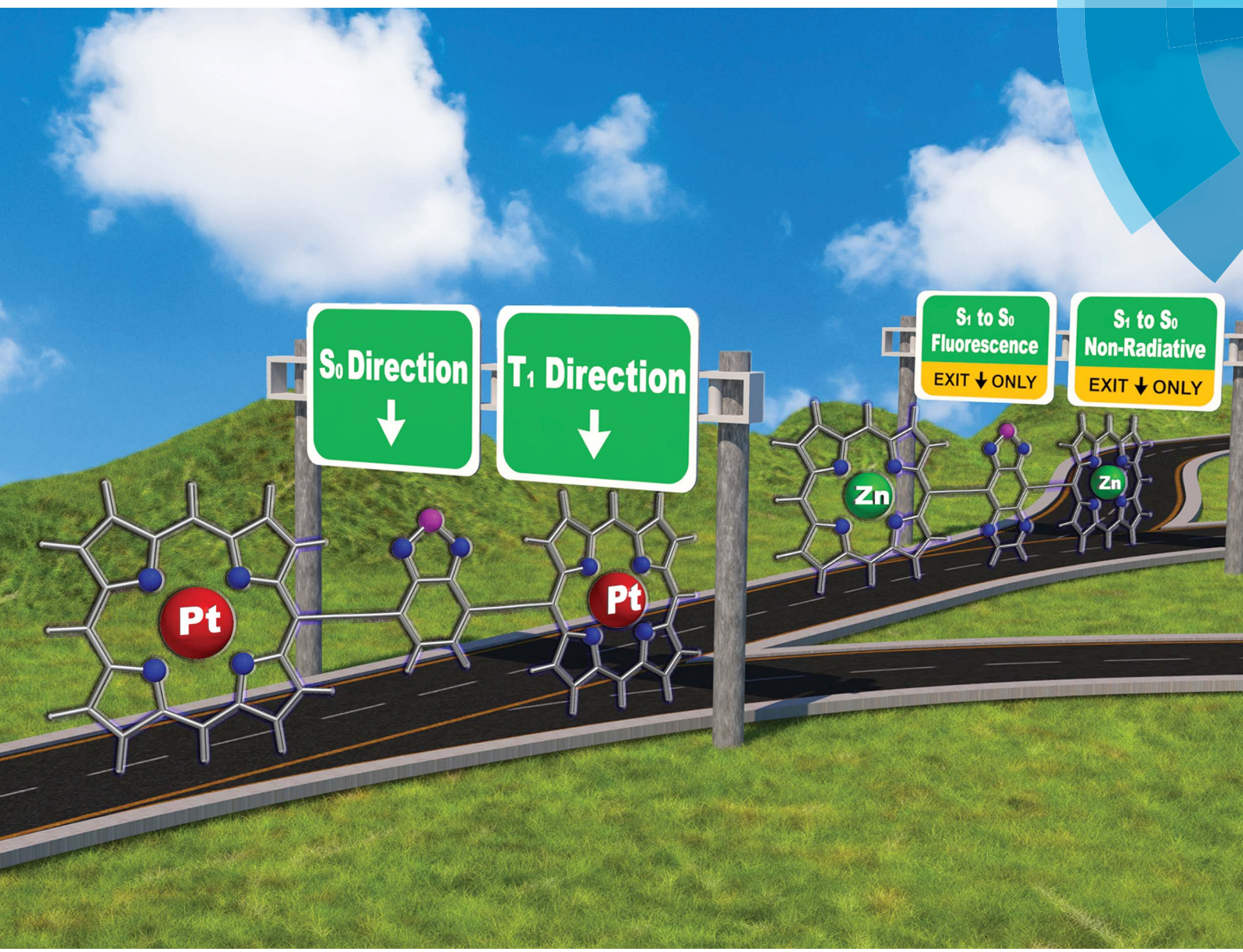

ISSN 2041-6539

ROYAL SOCIETY OF CHEMISTRY

EDGE ARTICLE

Michael J. Therien *et al.*

Controlling the excited-state dynamics of low band gap, near-infrared absorbers *via* proquinoidal unit electronic structural modulation

Chemical Science

EDGE ARTICLE

View Article Online
View Journal | View Issue

Check for updates

Cite this: *Chem. Sci.*, 2017, **8**, 5889

Controlling the excited-state dynamics of low band gap, near-infrared absorbers *via* proquinoidal unit electronic structural modulation†

Yusong Bai, Jeff Rawson, Sean A. Roget, Jean-Hubert Olivier, Jiaxing Lin, Peng Zhang, David N. Beratan and Michael J. Therien*

While the influence of proquinoidal character upon the linear absorption spectrum of low optical bandgap π-conjugated polymers and molecules is well understood, its impact upon excited-state relaxation pathways and dynamics remains obscure. We report the syntheses, electronic structural properties, and excited-state dynamics of a series of model highly conjugated near-infrared (NIR)-absorbing chromophores based on a (porphinato)metal(II)-proquinoidal spacer-(porphinato)metal(II) (**PM-Sp-PM**) structural motif. A combination of excited-state dynamical studies and time-dependent density functional theory calculations: (i) points to the cardinal role that excited-state configuration interaction (CI) plays in determining the magnitudes of $S_1 \rightarrow S_0$ radiative (k_r), $S_1 \rightarrow T_1$ intersystem crossing (k_{ISC}), and $S_1 \rightarrow S_0$ internal conversion (k_{IC}) rate constants in these **PM-Sp-PM** chromophores, and (ii) suggests that a primary determinant of CI magnitude derives from the energetic alignment of the **PM** and **Sp** fragment LUMOs (ΔE_L). These insights not only enable steering of excited-state relaxation dynamics of high oscillator strength NIR absorbers to realize either substantial fluorescence or long-lived triplets (τ_{T_1} > μs) generated at unit quantum yield (Φ_{ISC} = 100%), but also crafting of those having counter-intuitive properties: for example, while (porphinato) platinum compounds are well known to generate non-emissive triplet states (Φ_{ISC} = 100%) upon optical excitation at ambient temperature, diminishing the extent of excited-state CI in these systems realizes long-wavelength absorbing heavy-metal fluorophores. This work highlights approaches to: (i) modulate low-lying singlet excited-state lifetime over the picosecond-to-nanosecond time domain, (ii) achieve NIR fluorescence with quantum yields up to 25%, (iii) tune the magnitude of S_1–T_1 ISC rate constant from 10^9 to 10^{12} s^{-1} and (iv) realize T_1-state lifetimes that range from ~0.1 to several μs, for these model **PM-Sp-PM** chromophores, and renders new insights to evolve bespoke photophysical properties for low optical bandgap π-conjugated polymers and molecules based on proquinoidal conjugation motifs.

Received 13th May 2017
Accepted 6th June 2017

DOI: 10.1039/c7sc02150j

rsc.li/chemical-science

Open Access Article. Published on 07 June 2017. Downloaded on 1/5/2025 1:17:14 AM.
This article is licensed under a Creative Commons Attribution-NonCommercial 3.0 Unported Licence.

Introduction

Low optical bandgap π-conjugated polymers and molecules have fuelled spectacular developments in optical and optoelectronic technologies.[1] A common strategy to realize polymer bandgap reduction relies on augmenting the π-backbone quinoidal character. Introduction of so-called proquinoidal units into the conjugation main chain drives well understood perturbations to the ground-state electronic absorption spectrum, where augmented proquinoidal character diminishes both the optical (E_{op}) and potentiometric (E_p; $E_{1/2}^{0/+} - E_{1/2}^{-/0}$) band gaps of the material.[2] In contrast to the ground-state absorptive and electronic structural control enabled by proquinoidal motifs,[2c,d,g–j,3] considerably less insight exists concerning the impact of proquinoidal character on excited-state relaxation pathways and dynamics of extensively π-conjugated molecules and materials.

Control over the excited-state relaxation dynamics of highly conjugated NIR-absorbing materials would broadly boost their utility for optical and optoelectronic applications. For instance, long-wavelength optical power limiting (OPL) relies upon reverse-saturable absorption, demanding materials whose photoexcitation is followed by rapid intersystem crossing (ISC) with near-unit quantum yield to a long-lived triplet excited state.[1d,4] Triplet–triplet annihilation photon-upconversion (TTA-UC), which has applications that include solar energy harvesting, places a premium on enhancing near-infrared (NIR) absorptive oscillator strength and engineering ultrafast ISC.[5] In contrast, deep tissue-penetrating *in vivo* imaging requires extending the absorptive and emissive wavelengths of NIR fluorophores while maintaining large $S_1 \rightarrow S_0$ transition dipole moments.[1e,6] Advancing these applications motivates the development of design approaches to regulate the natures of

Department of Chemistry, French Family Science Center, Duke University, 124 Science Drive, Durham, North Carolina 27708-0346, USA. E-mail: Michael.therien@duke.edu

† Electronic supplementary information (ESI) available. See DOI: 10.1039/c7sc02150j

Open Access Article. Published on 07 June 2017. Downloaded on 1/5/2025 1:17:14 AM.
This article is licensed under a Creative Commons Attribution-NonCommercial 3.0 Unported Licence.

initially prepared photo-excited states and the subsequent relaxation dynamics of long-wavelength absorbers.

Here, we combine molecular design and synthesis, time-resolved spectroscopic methods, and quantum chemical analyses to delineate the excited-state properties of a series of model highly conjugated NIR-absorbing chromophores based on a (porphinato)metal(II)-spacer-(porphinato)metal(II) (**PM-Sp-PM**) structural motif[2c] in which: the porphyryl ligand is either electron rich (10,20-diarylporphyrin, **ArP**) or electron deficient (10,15,20-tris(perfluoroalkyl)porphyrin, **Rf$_3$P**), the central metal ion is **Zn(II)** or **Pt(II)**, and the proquinoidal **Sp** is either 4,7-diethynylbenzo[*c*][1,2,5]thiadiazole (**E-BTD-E**) or 4,9-diethynyl-6,7-dimethyl[1,2,5]thiadiazolo[3,4-*g*]quinoxaline (**E-TDQ-E**). Steady-state absorption, emission, and pump-probe transient absorption spectroscopic experiments, and time-dependent density functional theory (TD-DFT) computational studies, unambiguously correlate the extent of configuration interaction (CI) and charge transfer (CT) character of the initially prepared excited state with the relative magnitudes of $S_1 \rightarrow S_0$ radiative (k_r), $S_1 \rightarrow T_1$ intersystem crossing (k_{ISC}), and $S_1 \rightarrow S_0$ internal conversion (k_{IC}) rate constants. Collectively, these studies demonstrate how electronic modulation of proquinoidal conjugation motifs, conventionally utilized to regulate the ground-state absorptivity of low optical bandgap π-conjugated polymers and molecules, can also be exploited to steer their excited-state relaxation pathways. This work: (i) underscores how modulation of the extent of excited-state CI for conjugation motifs that rely on proquinoidal units can produce either exceptional NIR fluorophores or chromophores that generate long-lived electronically excited state triplets at high quantum yield, and (ii) describes a roadmap *via* which the relative magnitudes of k_r, k_{ISC}, and k_{IC} rate constants may be engineered to tightly control photophysical function of highly conjugated NIR-absorbing materials.

Results and discussion

Synthesis

Scheme 1 outlines the synthetic strategies for the **PM-Sp-PM** species, including **ArPM-Sp-ArPM** [**M** = **Zn(II)**, **Pt(II)**; **Sp** = **E-TDQ-E**, **E-BTD-E**], **Rf$_3$PZnE-TDQ-ERf$_3$PZn**, and **Rf$_3$PZnArPPtE-TDQ-ERf$_3$PZnArPPt**. Generally, the desired **PM-Sp-PM** supermolecular chromophores were prepared by the metal-mediated cross-coupling[7] of a mono *meso*-ethyne-functionalized (porphinato)metal(II) species with a dibrominated proquinoidal spacer moiety (Scheme 1). The key precursor compound **Rf$_3$PZnArPPtE** was prepared *via* a Pd^0-mediated coupling reaction involving **Rf$_3$PZnE** and **BrArPPtETIPS**, followed by deprotection of the triisopropylsilyl group. Chromophores featuring **ArPM-Sp-ArPM** molecular structures were isolated *via* column chromatography on silica using 2 : 3 CH_2Cl_2 : hexanes as the eluent, while for chromophores containing the **Rf$_3$PZn** fragment, 3 : 7 THF : hexanes was employed due to their solubility in this mobile phase. Size exclusion column chromatography with THF eluent was employed for purification of each chromophore after silica column chromatography. Scheme 2 displays the chemical structures for previously established oligo(porphinato)metal(II) compounds[8] that define key spectroscopic benchmarks for these newly designed **PM-Sp-PM** chromophores.

Steady-state absorption and emission spectroscopy of ArPM-Sp-ArPM chromophores

Steady-state electronic absorption and fluorescence spectra recorded for **ArPM-Sp-ArPM** species (**ArPZnE-BTD-EArPZn**,[2c] **ArPZnE-TDQ-EArPZn**,[2c] **ArPPtE-BTD-EArPPt**, and **ArPPtE-TDQ-**

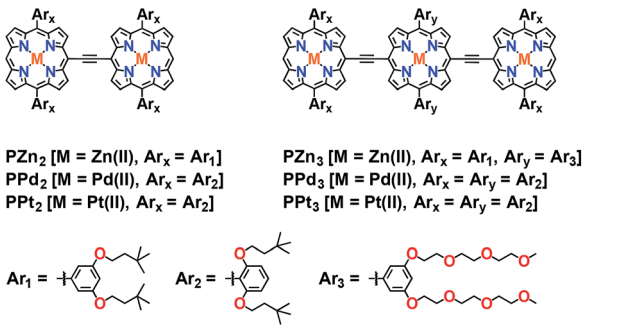

Scheme 2 Chemical structures for previously established oligo(porphinato)metal(II) chromophores.

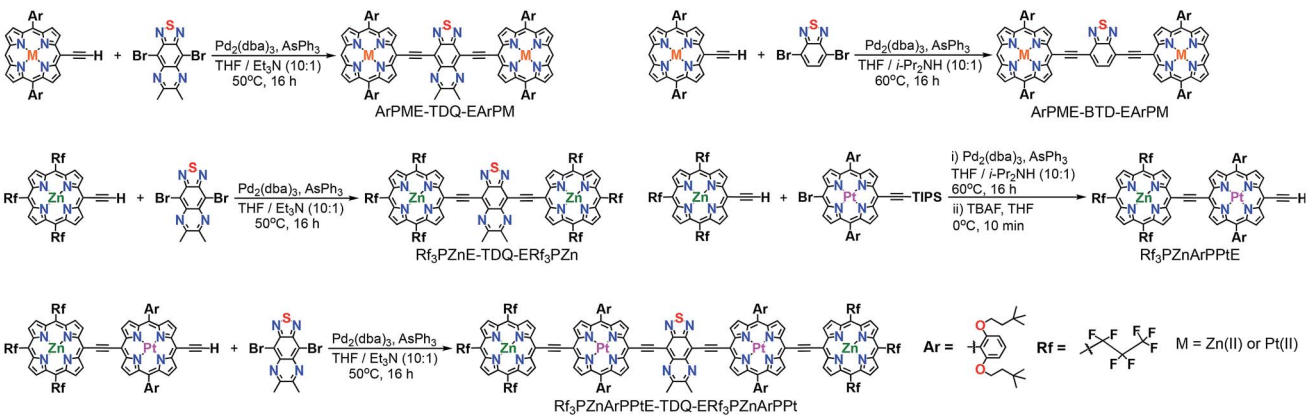

Scheme 1 Synthetic routes and chemical structures for PM-Sp-PM compounds.

 This journal is © The Royal Society of Chemistry 2017

Open Access Article. Published on 07 June 2017. Downloaded on 1/5/2025 1:17:14 AM.
This article is licensed under a Creative Commons Attribution-NonCommercial 3.0 Unported Licence.

EArPPt) are displayed in Fig. 1. The gross features of the electronic absorption spectra for these complexes resemble those of dimeric and multimeric porphyrin compounds that feature a *meso*-to-*meso* ethyne-linkage topology (**PZn$_n$** compounds), manifesting two distinct absorption manifolds that are derived from the porphyrin B- (Soret) ($S_0 \rightarrow S_2$) and Q-band ($S_0 \rightarrow S_1$) transitions.[8a–c,9] Previous investigations have demonstrated that **Sp** moieties modulate the respective **ArPZn-Sp-ArPZn** long axis-polarized Q state (Q_x) absorption maxima from 689 to 1006 nm, depending upon the extent of the quinoidal resonance contribution to the electronically excited singlet state.[2c] Further, semi-empirical electronic structure calculations and electrochemical data underscored the cardinal role that **ArPZn** and **Sp** fragment orbital energy differences played in fixing the radical cation and anion state energy levels in these **ArPZn-Sp-ArPZn** structures.[2c]

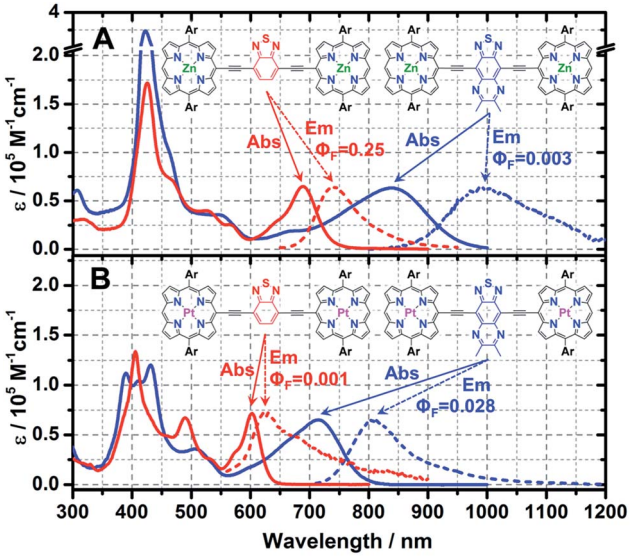

Fig. 1 Steady-state electronic absorption and emission spectra for: (A) ArPZnE-TDQ-EArPZn (blue colored lines, λ_{exc} = 750 nm for emission) and ArPZnE-BTD-EArPZn (red colored lines, λ_{exc} = 640 nm for emission): and (B) ArPPtE-TDQ-EArPPt (blue colored lines, λ_{exc} = 650 nm for emission) and ArPPtE-BTD-EArPPt (red colored lines, λ_{exc} = 540 nm for emission). Steady-state spectra were all acquired in THF solvent at ambient condition. Ar = 2′,6′-bis(3,3-dimethyl-1-butyloxy)phenyl.

A comparison of the Q-band regions in the electronic absorption spectra of **ArPZnE-BTD-EArPZn**, **ArPZnE-TDQ-EArPZn**, **ArPPtE-BTD-EArPPt**, and **ArPPtE-TDQ-EArPPt** reveals discrete effects correlated with the choice of spacer and (porphinato)metal(II) units. Compared with **ArPME-BTD-EArPM**, the **ArPME-TDQ-EArPM** analogues evince dramatically red-shifted Q_x-state absorption maxima and substantial oscillator strength (f) redistribution into the low-energy spectral domain [compound ($\lambda_{max}(S_0 \rightarrow S_1)$, $f_{600-1000\ nm}$): **ArPZnE-BTD-EArPZn** (689 nm, 0.455), **ArPPtE-BTD-EArPPt** (603 nm, 0.168), **ArPZnE-TDQ-EArPZn** (839 nm, 0.827), **ArPPtE-TDQ-EArPPt** (715 nm, 0.686); Table 1]. Furthermore, the Q_x-state absorption manifolds of **ArPME-TDQ-EArPM** species manifest much broader full width at half maxima (FWHM) and less discernable vibrational structures relative to those evinced by **ArPME-BTD-EArPM** chromophores [Q_x(FWHM): **ArPME-TDQ-EArPM** $\sim$ 2500 cm^{-1}; **ArPME-BTD-EArPM** $\sim$ 1100 cm^{-1}], suggesting that the **TDQ**-containing chromophores give rise to S_1 states with greater CT character.[2c,10] Compared to **ArPZn-Sp-ArPZn** compounds, the **ArPPt-Sp-ArPPt** chromophores display blue-shifted Q_x-state transition manifold maxima; this phenomenon is typical of hypsoporphyrin species and has been attributed to the efficient mixing of metal nd_π and porphyrin π^* orbitals.[8e,11]

ArPZnE-BTD-EArPZn and **ArPZnE-TDQ-EArPZn** exhibit markedly different Stokes shifts and fluorescence quantum yields (Φ_F) (Fig. 1) in THF solvent. While **ArPZnE-BTD-EArPZn** displays a relatively small Stokes shift ($\Delta\nu$ = 1019 cm^{-1}) and a large fluorescence quantum yield (Φ_F = 0.25) comparable to those of **PZn$_n$** chromophoric benchmarks (*e.g.* **PZn$_2$**: $\Delta\nu$ = 711 cm^{-1}, Φ_F = 0.16. **PZn$_3$**: $\Delta\nu$ = 806 cm^{-1}, Φ_F = 0.22; Scheme 2),[8d,9c] **ArPZnE-TDQ-EArPZn** exhibits a significant Stokes shift of 1869 cm^{-1} and negligible fluorescence (Φ_F = 0.003). Furthermore, the Stokes shift and fluorescence quantum yield of **ArPZnE-BTD-EArPZn** show modest solvent dependence [*e.g.*, toluene

Table 1 Low-energy absorption and fluorescence band maxima, FWHM values, Stokes shifts, and integrated absorptive oscillator strengths for PM-Sp-PM chromophores over the 600–1000 nm wavelength range

	λ_{max}/nm (FWHM/cm^{-1})			
Chromophores	$S_0 \rightarrow S_1$	$S_1 \rightarrow S_0$	Stokes shift[a]/cm^{-1}	Oscillator strength in red-to-NIR[b]
ArPZnE-TDQ-EArPZn	839 (2510)	995 (1778)	1869	0.827
ArPZnE-BTD-EArPZn	689 (1180)	741 (1382)	1019	0.455
ArPPtE-TDQ-EArPPt	715 (2415)	810 (1530)	1640	0.686
ArPPtE-BTD-EArPPt	603 (1061)	629 (1579)	686	0.168
Rf$_3$PZnE-TDQ-ERf$_3$PZn	705 (1163)	750 (1370)	851	0.451
Rf$_3$PZnArPPtE-TDQ-EArPPtRf$_3$PZn	755 (1738)	813 (1432)	945	1.809

[a] Stokes shift corresponds to the energy difference between the low-energy transition (Q_x) absorption and fluorescence maxima. [b] Integrated oscillator strengths (f) were calculated based on the following expression: $f = 4.3 \times 10^{-9} \int \varepsilon d\nu$, where ε is the experimental extinction coefficient, and ν is the energy (in wave numbers) of the absorption. Oscillator strengths were calculated over the following spectral domains: **ArPZnE-TDQ-EArPZn** (600–1000 nm); **ArPZnE-BTD-EArPZn** (600–800 nm); **ArPPtE-TDQ-EArPPt** (600–850 nm); **ArPPtE-BTD-EArPPt** (600–700 nm); **Rf$_3$PZnE-TDQ-ERf$_3$PZn** (600–850 nm); **Rf$_3$PZnArPPtE-TDQ-EArPPtRf$_3$PZn** (600–950 nm).

Open Access Article. Published on 07 June 2017. Downloaded on 1/5/2025 1:17:14 AM. This article is licensed under a Creative Commons Attribution-NonCommercial 3.0 Unported Licence.

($\Delta\nu = 522\ cm^{-1}$, $\Phi_F = 0.27$)] (Fig. S1†); in contrast, a substantial solvent-dependence of the Stokes shift and fluorescence quantum yield are evinced for **ArPZnE-TDQ-EArPZn**, with less polar solvent driving smaller Stokes shifts and significantly enhanced fluorescence quantum yields [toluene ($\Delta\nu_{Stokes} = 771\ cm^{-1}$, $\Phi_F = 0.02$) *vs.* THF ($\Delta\nu_{Stokes} = 1869\ cm^{-1}$, $\Phi_F = 0.003$)] (Fig. S2†). These observations underscore the differing CT characters of the **ArPZnE-TDQ-EArPZn** and **ArPZnE-BTD-EArPZn** Q_x-states; as **ArPZnE-TDQ-EArPZn** exhibits substantial CT character, the reorganization energy associated with excited-state solvent relaxation is magnified.[9c,12]

Upon metal center substitution from zinc(II) to platinum(II), **ArPPtE-BTD-EArPPt** manifests weak fluorescence centered at 629 nm ($\Delta\nu = 686\ cm^{-1}$, $\Phi_F = 0.001$) in deoxygenated solution at ambient temperature, and phosphorescence centered at 845 nm ($\Delta\nu = 4750\ cm^{-1}$) (Fig. S3†). Such emissive properties are similar to those observed in oligomeric (porphinato)palladium(II)/platinum(II) compounds (**PM$_3$**, **M** = **Pd** or **Pt**; Scheme 2), where phosphorescence and very weak fluorescence (77 K) are simultaneously evinced (**PPd$_3$**: $\lambda_{S_1\rightarrow S_0}(max) = 747$ nm; $\lambda_{T_1\rightarrow S_0}(max) = 828$ nm; **PPt$_3$**: $\lambda_{S_1\rightarrow S_0}(max) = 740$ nm; $\lambda_{T_1\rightarrow S_0}(max) = 800$ nm).[8e] In contrast, **ArPPtE-TDQ-EArPPt** maintains one constant emission band centered at 810 nm, regardless of the solution oxygen content (Fig. S4†). Note that no additional emission band can be observed in deoxygenated samples of **ArPPtE-TDQ-EArPPt** even at low temperature (77 K, Fig. S5†). In light of the magnitude of the Stokes shift ($\Delta\nu = 1530\ cm^{-1}$) and the measured lifetime of this chromophore (τ = 310 ps, Fig. S6E†), we denote the **ArPPtE-TDQ-EArPPt** emission band centered at 810 nm as fluorescence. Given the (porphinato)-platinum(II) components of this chromophore, it is recognized that the low-lying emissive state of **ArPPtE-TDQ-EArPPt** may be best described as a "sing–triplet". In this regard, we emphasize that although the "fluorescence", "phosphorescence", "S_1", and "T_1" labels are preserved throughout this report for describing the respective higher and lower energy emissive states of the platinum-containing **PM-Sp-PM** compounds, they suggest only the dominant characters of these excited states. Note that the fluorescence quantum yield determined for **ArPPtE-TDQ-EArPPt** (2.8%) is unusually large, considering that platinum atoms typically promote strong spin–orbit coupling, resulting in near-unit $S_1 \rightarrow T_1$ ISC quantum yields (Φ_{ISC} values) in classic (porphinato)platinum(II) compounds.[8e,13] The emissive properties observed for **ArPPtE-TDQ-EArPPt** suggest an unusually low Φ_{ISC} value relative to the **ArPPtE-BTD-EArPPt** chromophore (*vide infra*).

Femtosecond pump-probe transient absorption spectroscopy of ArPM-Sp-ArPM

The femtosecond transient absorption spectra recorded at selected time delays for **ArPM-Sp-ArPM** chromophores are displayed in Fig. 2. The early time-delay (<1 ps) transient spectra of these **ArPM-Sp-ArPM** chromophores share several common features that resemble the transient spectral signatures of ethyne-bridged multimeric (porphinato)zinc(II) structures (**PZn$_n$**, n = 2, 3; Scheme 2).[9a,c] These include: (i) bleaching signals in the Soret and Q_x band regions, (ii) weak transient absorptions between the two dominant ground-state absorption bleaching signatures, and (iii) intense NIR $S_1 \rightarrow S_n$ transient absorption manifolds that feature extraordinary spectral breadth.[8d,e,9c]

Conventional **PZn$_n$** excited-state dynamics include fast $S_2 \rightarrow S_1$ internal conversion (<1 ps),[9a] nanosecond timescale S_1 state lifetimes,[8e,9c] and small Stokes shifts in virtually all solvents;[8d,9c] this latter point suggests minimal degrees of solvent

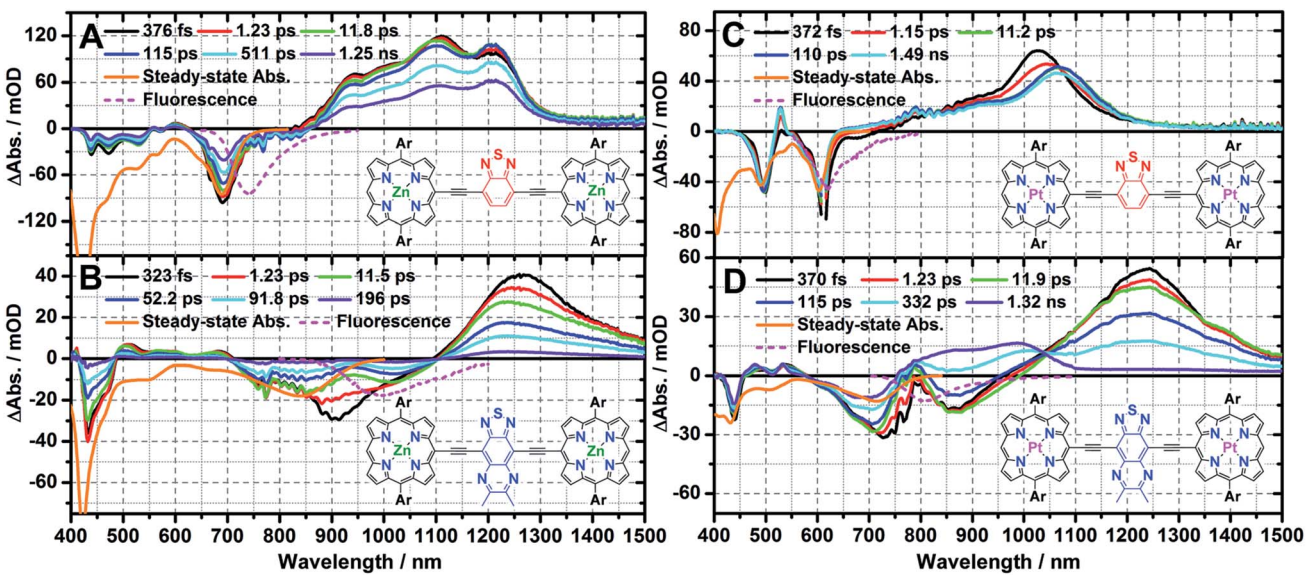

Fig. 2 Pump-probe transient absorption spectra recorded at several time delays for (A) **ArPZnE-BTD-EArPZn** (λ_{exc} = 660 nm), (B) **ArPZnE-TDQ-E ArPZn** (λ_{exc} = 900 nm), (C) **ArPPtE-BTD-EArPPt** (λ_{exc} = 610 nm), and (D) **ArPPtE-TDQ-EArPPt** (λ_{exc} = 750 nm). Experimental conditions: solvent = THF; ambient temperature; magic angle polarization. Steady-state absorption (orange solid line) and fluorescence (magenta dash line) are provided as inverted spectra. Ar = 2′,6′-bis(3,3-dimethyl-1-butyloxy)phenyl.

 This journal is © The Royal Society of Chemistry 2017

Open Access Article. Published on 07 June 2017. Downloaded on 1/5/2025 1:17:14 AM. This article is licensed under a Creative Commons Attribution-NonCommercial 3.0 Unported Licence.

repolarization and inner-sphere chromophore nuclear reorganization are associated with excited-state relaxation of these species. Furthermore, upon metal center substitution with palladium(II) or platinum(II), the corresponding **PPd$_n$**, or **PPt$_n$** chromophores (Scheme 2) manifest ultrafast intersystem crossing on sub-picosecond to picosecond timescales.[8e] For corresponding **ArPM-Sp-ArPM** species, however, it is clear that the proquinoidal spacer units regulate electronically excited-state electron density spatial distributions (Fig. 2).

Femtosecond transient absorption spectroscopy of ArPZn-Sp-ArPZn

A global fit of the NIR transient absorption dynamics observed following excitation ($\lambda_{exc} = 660$ nm), evinces three characteristic relaxation processes: 760 ± 90 fs, 24 ± 5 ps, 1.75 ± 0.1 ns (Fig. S8A†). The 760 fs and 24 ps components are assigned to respective solvent relaxation, and structural relaxation processes associated with torsional dynamic about the ethyne-Sp-ethyne **ArPZn**-to-**ArPZn** linkage; these dynamics have been discussed in detail for closely related structures.[9a,c] The 1.75 ns component corresponds with ground-state recovery and is assigned to the intrinsic S_1 state lifetime, in close agreement with the fluorescence lifetime determined by streak-scope (τ_F = 1.67 ns, Fig. S6C†). Consistent with the insensitivity of the Stokes shift and fluorescence quantum yield to solvent polarity, the S_1 state lifetime of **ArPZnE-BTD-EArPZn** manifests minimal variation with solvent dielectric constant [*e.g.* THF ($\tau_F = 1.67$ ns) *vs.* toluene ($\tau_F = 1.61$ ns, Fig. S6D†)], suggesting the electronically excited-state nature of **ArPZnE-BTD-EArPZn** features negligible CT character.

The excited-state relaxation dynamics of **ArPZnE-TDQ-EArPZn** are also multiexponential in nature. Global fitting of the NIR spectral regime transient dynamical data acquired for **ArPZnE-TDQ-EArPZn** evinces three relaxation processes: 950 ± 120 fs, 12 ± 2 ps, and 87 ± 6 ps (Fig. S8B†). While the 950 fs and 12 ps components correspond, respectively, to the solvent relaxation and structural relaxation dynamics, the 87 ps component is very close to the streak-scope determined fluorescence lifetime (τ_F = 76 ps) of **ArPZnE-TDQ-EArPZn** (Fig. S6A†), and is thus assigned to the intrinsic singlet excited-state lifetime. Notably, the THF solvent relaxation component mirrors the timescale for the time-dependent red shift of the stimulated emission from 910 to 1020 nm ($\Delta\nu = 1185$ cm^{-1}). This dynamic Stokes shift, absent for **ArPZnE-BTD-EArPZn**, indicates substantial displacement between the ground- and singlet excited-state potential energy surfaces along the solvation coordinate,[10b,14] congruent with the marked solvent-dependent **ArPZnE-TDQ-EArPZn** Stokes shifts observed by steady-state emission spectroscopy (*vide supra*). Additionally, the S_1 state lifetime (τ_{S_1} = 87 ps) of **ArPZnE-TDQ-EArPZn** is much shorter than that of **ArPZnE-BTD-EArPZn**, and depends strongly on solvent dielectric constant (ε_s). For example, the τ_F determined for **ArPZnE-TDQ-EArPZn** measured in toluene solvent (~506 ps, Fig. S6B†) is nearly 1 order of magnitude larger than that found in THF. As such, the calculated $S_1 \rightarrow S_0$ internal conversion rate constants for **ArPZnE-TDQ-EArPZn** in THF and toluene differ markedly [k_{IC}(THF) = 1.15 × 10^{10} s^{-1} *vs.* k_{IC}(toluene) = 1.94 × 10^9 s^{-1}], highlighting the acceleration of the nonradiative decay process in polar solvent: since the Q_x-state transition features substantial CT character, solvent dipole reorientation dramatically stabilizes the polarized S_1 state of **ArPZnE-TDQ-EArPZn**, decreasing the $S_1 \rightarrow S_0$ transition oscillator strength [Φ_F(THF) = 0.003 *vs.* Φ_F(toluene) = 0.02].

Femtosecond transient absorption spectroscopy of ArPPt-Sp-ArPPt

A global fit of the time-dependent vis-NIR transient dynamical data acquired for **ArPPtE-BTD-EArPPt** following excitation at 610 nm evinces two relaxation processes: 960 ± 120 fs, 1.90 ± 0.13 ns (Fig. S8C†). Note that at an early time delay ($t_{delay} \sim 1$ ps), the initially prepared **ArPPtE-BTD-EArPPt** electronically excited state has already evolved to a long-lived excited state that persists beyond the delay limit of the femtosecond pump-probe instrument. Nanosecond pump-probe transient absorption measurements determine that the lifetime of this long-lived excited state is 2.5 μs, which is reduced to 0.24 μs under oxygenated conditions (Fig. S7C and D†), suggesting that the long-lived excited state is triplet in nature. In this regard, the ultrafast component (960 fs) observed in the femtosecond transient dynamics corresponds to an ISC process, while the 1.90 ns component corresponds to the slow decay of **ArPPtE-BTD-EArPPt** triplet excited state. Furthermore, the decay-associated spectra (DAS, Fig. S8†) connected with the ultrafast component manifests an S-like shape in the 900–1200 nm domain, displaying a decay on the blue side and rise on the red side of the transient, suggesting unit quantum yield $S_1 \rightarrow T_1$ conversion (*i.e.* $\tau_{S_1} \approx \tau_{ISC} \sim 960$ fs, $\Phi_{ISC} \sim 100\%$). The ultrafast $S_1 \rightarrow T_1$ conversion and near-unit ISC quantum yield displayed by **ArPPtE-BTD-EArPPt** are similar to those evinced by **PPt$_n$** compounds (Table 2).[8e]

In contrast to the ultrafast ISC rate constant exhibited by **ArPPtE-BTD-EArPPt**, the **ArPPtE-TDQ-EArPPt** analogue manifests dramatically different excited-state relaxation dynamics. Three time constants were obtained from fitting the **ArPPtE-TDQ-EArPPt** transient data acquired following Q-band excitation (λ_{exc} = 750 nm): 1.05 ± 0.15 ps, 15 ± 2 ps, 330 ± 15 ps (Fig. S8D†). Analogous to the characteristic relaxation times evinced for **ArPZn-Sp-ArPZn** chromophores, the two fast time constants (1.05 ps and 15 ps) correspond respectively to established THF solvational and structural relaxation dynamics. The 330 ps component is comparable to the streak-scope determined fluorescence lifetime of **ArPPtE-TDQ-EArPPt** (τ_F = 310 ps, Fig. S6E†), and is thus assigned to the intrinsic S_1 state lifetime. While the **ArPZnE-TDQ-EArPZn** transient spectra feature complete ground state recovery within 200 ps, those of **ArPPtE-TDQ-EArPPt** evolve at long-time delays to give rise to a new transient absorption band that spans the 800–1050 nm spectral domain. This transient absorption manifold persists beyond the delay limit of the femtosecond instrument (Fig. 2D). Nanosecond transient absorption spectroscopy determines the lifetime of this long-lived excited state to be 250 ns in deoxygenated solutions, while in ambient atmosphere saturated

Open Access Article. Published on 07 June 2017. Downloaded on 1/5/2025 1:17:14 AM. This article is licensed under a Creative Commons Attribution-NonCommercial 3.0 Unported Licence.

Table 2 Excited-state relaxation dynamical data, fluorescence quantum yields, and intersystem crossing quantum yields for PM-Sp-PM chromophores

Chromophores	τ_{S_1}/ns	Relaxation rate from S_1[a]/s^{-1}			Φ_F[b]	Φ_{ISC}[c]
		$k_{IC}(S_1 \rightarrow S_0)$	$k_F^0(S_1 \rightarrow S_0)$	$k_{ISC}(S_1 \rightarrow T_1)$		
ArPZnE-TDQ-EArPZn	0.087	1.15×10^{10}	3.10×10^{7}	$\leq 10^{7}$	0.003	~0
ArPZnE-BTD-EArPZn	1.750	3.82×10^{8}	1.43×10^{8}	8.57×10^{7}	0.25	0.15
ArPPtE-TDQ-EArPPt	0.310	1.51×10^{9}	9.15×10^{7}	1.67×10^{9}	0.028	0.50
ArPPtE-BTD-EArPPt	0.001	$\leq 10^{8}$	$\sim 10^{8}$	1.04×10^{12}	0.001	~1
Rf_3PZnE-TDQ-ERf_3PZn	0.785	9.04×10^{8}	1.53×10^{8}	2.17×10^{8}	0.12	0.17
Rf_3PZnArPPtE-TDQ-EArPPtRf_3PZn	0.108	2.36×10^{9}	1.39×10^{8}	6.76×10^{9}	0.015	0.73

[a] k_{IC} denotes the $S_1 \rightarrow S_0$ nonradiative decay rate constant, k_F^0 denotes the intrinsic fluorescence rate constant, k_{ISC} denotes the $S_1 \rightarrow T_1$ intersystem crossing rate constant. Excited-state relaxation rate constants were calculated based on the following equations: $\tau_{S_1} = 1/(k_{IC} + k_F^0 + k_{ISC})$, $\Phi_F = k_F^0 \times \tau_{S_1}$, $\Phi_{ISC} = k_{ISC} \times \tau_{S_1}$, since τ_{S_1}, Φ_F, and Φ_{ISC} can all be experimentally acquired, therefore, rate constants k_{IC}, k_F^0, and k_{ISC} can be calculated. [b] Fluorescence quantum yields were determined relative to bis[(porphinato)zinc(II)] (**PZn_2**) in THF (0.16). [c] Φ_{ISC} were determined based on femtosecond transient absorption spectra, for details see ESI.

solutions it is reduced to 140 ns (Fig. S7A and B†), suggesting that the corresponding excited state is dominated by triplet character. Femtosecond timescale transient absorption spectral data allow direct evaluation of the $S_1 \rightarrow T_1$ ISC quantum yield and rate constant ($\Phi_{ISC} \sim 51\%$; $k_{ISC} \sim 1.67 \times 10^9\ s^{-1}$) for **ArPPtE-TDQ-EArPPt** (ESI; Table 2†). The excited-state relaxation dynamics of **ArPPtE-TDQ-EArPPt** thus contrast those evinced in classic oligomeric highly conjugated (porphinato)platinum(II) species where near-unit ISC quantum yields and sub-picosecond ISC time constants are manifested.[8e] Also note that the S_1 state lifetime of **ArPPtE-TDQ-EArPPt** is about four times longer than that of its **ArPZnE-TDQ-EArPZn** analogue, whereas **PPt_n** evince significantly diminished S_1 state lifetimes relative to the corresponding **PZn_n** chromophores due to ultrafast $S_1 \rightarrow T_1$ ISC dynamics (Scheme 2).[8d,e] In this regard, the longer S_1 state lifetime (Table 2) of **ArPPtE-TDQ-EArPPt** relative to **ArPZnE-TDQ-EArPZn** originates from two factors: (i) diminution of the nonradiative decay rate constant as the optical bandgap is widened when platinum(II) replaces zinc(II) in this chromophoric motif, and (ii) an unconventionally slow ISC rate constant. The origin of this slow ISC will be discussed in the context of TD-DFT calculations (*vide infra*).

These data (Fig. 1 and 2; Tables 1 and 2) demonstrate that varying the nature of the intervening proquinoidal spacer units drives substantially different absorptive and excited-state dynamical properties in **ArPM-Sp-ArPM** chromophores: (i) **ArPZn-Sp-ArPZn** chromophores, such as **ArPZnE-TDQ-EArPZn**, having significant excited-state proquinoidal character, exhibit broad long-wavelength absorptive manifolds and substantial NIR oscillator strength, negligible ($\Phi_F < 0.01$) fluorescence, and short-lived (~tens of ps) singlet excited state lifetimes. (ii) **ArPZn-Sp-ArPZn** chromophores, such as **ArPZnE-BTD-EArPZn**, that feature less electronically excited-state proquinoidal character, exhibit narrower long-wavelength absorptive manifolds and less substantial NIR oscillator strength, long-lived (ns) S_1 states and large ($\Phi_F \sim 0.25$) fluorescence quantum yields. (iii) **ArPPt-Sp-ArPPt** chromophores, characterized by **ArPPtE-TDQ-EArPPt** and **ArPPtE-BTD-EArPPt**, evince similar dependences of absorptive oscillator strength distribution upon the nature of the proquinoidal spacer, but show an unusual dependence of the degree of electronically excited-state proquinoidal character upon the magnitude of k_{ISC}: **ArPPtE-BTD-EArPPt**, which features a modest extent of excited-sate proquinoidal character, features a $S_1 \rightarrow T_1$ ISC rate constant ($k_{ISC} = 1.04 \times 10^{12}\ s^{-1}$) three orders of magnitude greater than that for **ArPPtE-TDQ-EArPPt**. The origins of these disparate photophysical properties modulated by these **Sp** units are explored below using TD-DFT calculations.

Computed electronic structures of ArPM-Sp-ArPM chromophores

The differing S_1 state CT characters of these **ArPM-Sp-ArPM** chromophores are underscored by population analyses of their frontier orbitals (FOs) and the transition matrix eigenvectors computed by TD-DFT methods (Fig. 3). The S_1 state of **ArPZnE-TDQ-EArPZn** is dominated (~80%) by the HOMO $\rightarrow$ LUMO configuration, where ~30% of the HOMO wavefunction amplitude and >70% of the LUMO amplitude is assigned to atoms in the **TDQ** spacer (see ESI† for molecular orbital population analyses). Photo-excitation of the **ArPZnE-TDQ-EArPZn** Q_x-band region, thus, redistributes electron density from the **ArPZn** to the **TDQ** unit, resulting in a delocalized S_1 state with substantial CT character. In contrast, **ArPZnE-BTD-EArPZn** manifests an S_1 state composed of multiple single-excitation configurations that involve FOs from HOMO−3 to LUMO+3, where the shares of HOMO and LUMO wavefunction amplitudes that can be assigned to **ArPZn** and **TDQ** subunits are comparable. These data indicate that the S_1 state for **ArPZnE-BTD-EArPZn** exhibits negligible CT character and substantial CI, more akin to classic porphyrin $\pi \rightarrow \pi^*$ transitions and those characteristic of **PZn_n** supermolecular chromophores.[8a–c,9c] These computational figures buttress the finding that the **ArPZnE-TDQ-EArPZn** Q_x transition has greater quinoidal character than that of **ArPZnE-BTD-EArPZn**,[2c] as demonstrated by analyses of the Q_x manifold FWHM and vibronic structures, fluorescence quantum yields, and the dynamic and solvent dependent Stokes shifts exhibited by these chromophores.

The contrasts outlined above regarding the S_1 state CT characters of the (porphinato)zinc(II) compounds are sustained

 This journal is © The Royal Society of Chemistry 2017

Open Access Article. Published on 07 June 2017. Downloaded on 1/5/2025 1:17:14 AM.
This article is licensed under a Creative Commons Attribution-NonCommercial 3.0 Unported Licence.

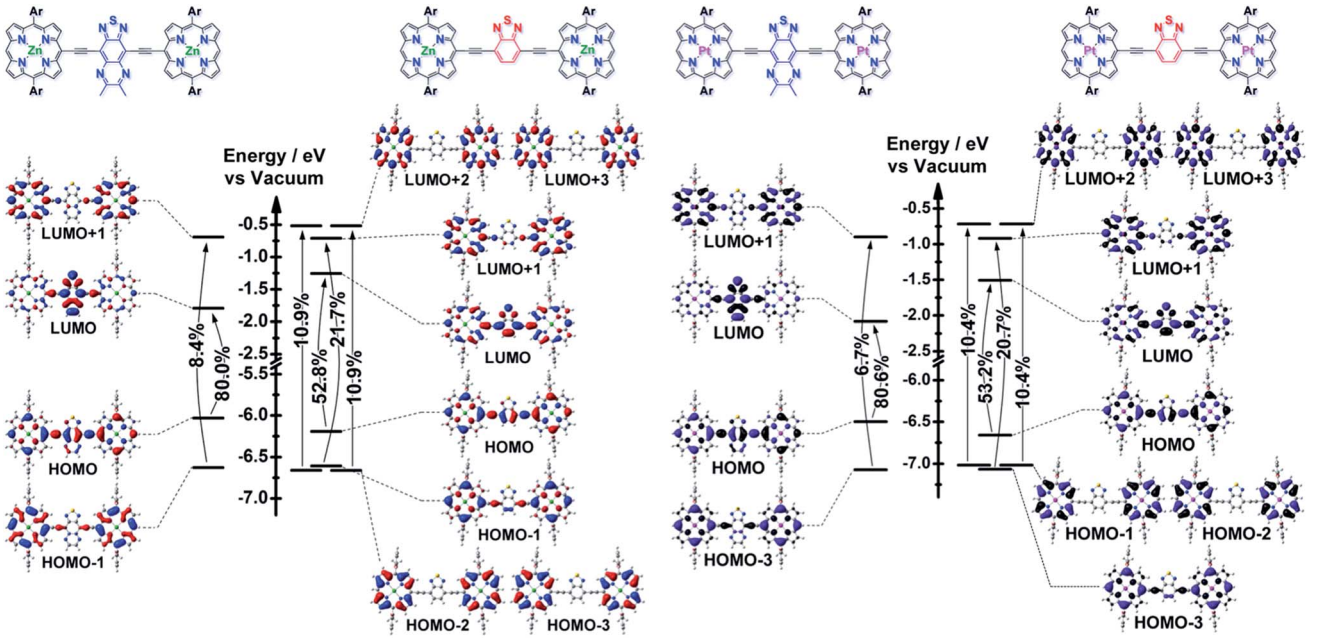

Fig. 3 TD-DFT determined energy level diagrams and frontier molecular orbitals for ArPM-Sp-ArPM [M = Zn(II) or Pt(II), Sp = E-TDQ-E, or E-BTD-E], with arrows depicting the one-electron configurations that contribute most significantly to the low-energy (Q_x) transitions. Calculations were performed at the M11/6-311g(d) theory level.

in their (porphinato)platinum(II) counterparts. A further distinction that may be drawn for these latter **ArPPtE-TDQ-EArPPt** and **ArPPtE-BTD-EArPPt** chromophores is that a lesser share of the S_1 state wavefunction amplitude lies proximal to the platinum atom for the **TDQ**-based compound than for the **BTD**-based analogue. Note that the **ArPPtE-TDQ-EArPPt** $S_0 \rightarrow S_1$ transition is mainly described by the HOMO $\rightarrow$ LUMO configuration, and population analysis demonstrates that the (porphinato)platinum(II)-derived electron density contributes ~23% to the **ArPPtE-TDQ-EArPPt** LUMO amplitude. In contrast, the **ArPPtE-BTD-EArPPt** $S_0 \rightarrow S_1$ transition features the interaction of several configurations involving FOs beyond the HOMO and LUMO, and all of the virtual FOs evince dominant (>50%) wavefunction amplitude assigned to the (porphinato)platinum(II) fragment. These population analyses rationalize the correlation of large k_{ISC} for the **ArPPtE-BTD-EArPPt** S_1 state with its strong CI character, and smaller k_{ISC} for the **ArPPtE-TDQ-EArPPt** S_1 states with its strong CT character: as ISC can be induced by spin–orbit coupling (a local effect induced by wavefunction density proximal to a heavy atom),[10a,15] it is clear that the wavefunction spatial distribution of the initially prepared singlet excited state of **ArPPtE-BTD-EArPPt** is responsible for its considerably greater S_1–T_1 mixing relative to that manifested for **ArPPtE-TDQ-EArPPt**.

Schematic potential energy surfaces summarizing the spectroscopic and dynamical data, and computed electronic structures for ArPME-Sp-EArPM chromophores

The spectroscopic, dynamical, and computational results for these **ArPME-Sp-EArPM** structures can be schematically illustrated using a series of qualitative potential energy surfaces as displayed in Scheme 3. In these schematic illustrations, the free energies of **ArPM-Sp-ArPM** chromophores in their ground states and low-lying singlet excited states are given as functions of a solvation coordinate, as spectroscopic and dynamical investigations indicate solvation dynamics play a prominent role in determining the excited-state relaxation pathways. TD-DFT calculations show that the **ArPME-TDQ-EArPM** S_1 states feature stronger proquinoid contributions and greater CT character than those of **ArPME-BTD-EArPM** analogues (Fig. 3). The CT character of the **ArPME-TDQ-EArPM** Franck–Condon state initiates solvent dipolar reorientation, which in turn augments excited-state electronic polarization. The evolving solvent reorganization creates a ladder of stabilized states with progressively enhanced CT character relative to the initially prepared S_1 state, funnelling excited-state energy through $S_1 \rightarrow S_0$ nonradiative conversion that competes with $S_1 \rightarrow T_1$ ISC (Scheme 3A). In this regard, note that the 1 ps characteristic solvent relaxation timescale (marked on potential energy surfaces for **ArPME-TDQ-EArPM**, Scheme 3A and C) corresponds to the timescale of the potential energy curve displacement (Δq) dynamics between S_0 and S_1 states that are driven along the solvent coordinate. The $S_0 \rightarrow S_1$ vertical transition of **ArPPtE-TDQ-EArPPt** manifests a lower degree of CI relative to that for **ArPPtE-BTD-EArPPt** (*vide supra*), and the major single-excitation configuration involves virtual FOs featuring spacer-dominant (~77%) electron density, resulting in diminished S_1–T_1 mixing (Scheme 3C), and hence the experimentally observed slow ISC rate constant ($1.67 \times 10^9\ s^{-1}$). In contrast, the low-energy transition for **ArPPtE-BTD-EArPPt** exhibits a higher degree of CI, and (porphinato)platinum(II)-derived electron density makes prominent (>50%) contributions to the

Open Access Article. Published on 07 June 2017. Downloaded on 1/5/2025 1:17:14 AM.
This article is licensed under a Creative Commons Attribution-NonCommercial 3.0 Unported Licence.

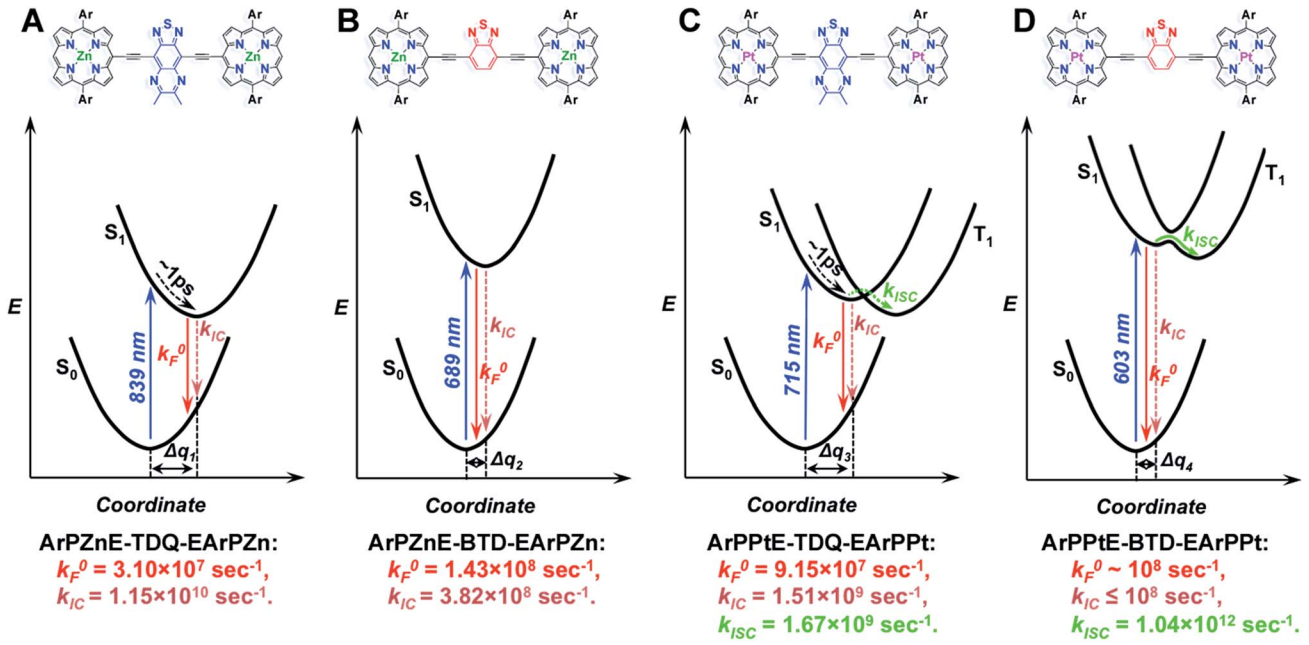

Scheme 3 Schematic potential energy surfaces summarizing the spectroscopic and dynamical features, and computed electronic structures, for ArPME-Sp-EArPM chromophores [M = Zn(II) or Pt(II), Sp = thiadiazoloquinoxaline (TDQ), or benzothiadiazole (BTD)].

amplitudes of all the **ArPPtE-BTD-EArPPt** virtual orbitals involved in the corresponding transition, relative to that in the **ArPPtE-BTD-EArPPt** chromophore, thus giving rise to stronger S_1–T_1 mixing and the ultrafast ISC rate constant (1.04×10^{12} s^{-1}) (Scheme 3D). Moreover, as the nature of the initially prepared S_1 state of **ArPPtE-BTD-EArPPt** is barely perturbed by solvent dynamics, $S_1 \rightarrow T_1$ ISC dominates excited-state relaxation processes, giving rise to the near-unity Φ_{ISC} in **ArPPtE-BTD-EArPPt**.

Relative frontier orbital energies of ArPM and spacers, and implications for new chromophore designs

The disparate CT characters of the **ArPME-TDQ-EArPM** and **ArPME-BTD-EArPM** S_1 states trace their origins to relative (porphinato)metal and spacer fragment FO energies; DFT calculations thus suggest rules for the rational engineering of excited-state dynamics in these supermolecular chromophores (Fig. 4). Here, a critical distinction is the energetic alignment of the **ArPM** and **Sp** fragment LUMOs (ΔE_L). For **ArPME-BTD-EArPM** compounds, which feature multiconfigurational S_1 states of modest CT character, ΔE_L between **ArPME** and **E-BTD-E** is smaller than 0.3 eV. For **ArPME-TDQ-EArPM** chromophores, which feature HOMO $\rightarrow$ LUMO-dominated S_1 states of substantial CT character, ΔE_L is larger than 1 eV. If the extent of CT character and degree of CI that describe the S_1 states of **ArPME-Sp-EArPM** chromophores define the dominant factors that determine their ISC rate constants and fluorescence quantum yields, then minimizing ΔE_L for **ArPZnE-Sp-EArPZn** chromophores will be the key to designing new long wavelength fluorophores, while minimizing ΔE_L for **ArPPtE-Sp-EArPPt** chromophores will enable elucidation of NIR absorbers that manifest substantial ISC quantum yields.

Supermolecules built from the **TDQ** spacer and porphyrin fragments endowed with LUMO energies that are substantially more stable than those of the *meso*-aryl derivatives mentioned so far permit the validation of this hypothesis. An established approach that uniformly stabilizes porphyrin macrocycle FOs by an inductive σ-electron withdrawing effect exploits *meso*-perfluoroalkyl substitution.[8c,16] The recently described electron-deficient *meso*-tris(perfluoroalkyl)porphyrin **Rf_3PZnE** is an ideal building for this purpose, as its HOMO and LUMO are both substantially stabilized relative to those of the [(5,-10,20-diphenylporphinato)zinc(II)]ethynyl (**ArPZnE**) unit (Fig. 4).[17] Furthermore, as the computed **Rf_3PZnArPPtE** LUMO is energetically close to that of **Rf_3PZnE** (Fig. 4), the **Rf_3PZnArPPtE-TDQ-EArPPtERf_3PZn** compound was designed with the expectation that it would display attenuated electronically excited-state proquinoidal character compared to **ArPPtE-TDQ-EArPPt**, and thus an ISC rate constant substantially larger than that of the parent chromophore **ArPPtE-TDQ-EArPPt**. Likewise, **Rf_3-PZnE-TDQ-ERf_3PZn** was designed with the expectation that this electronic structural engineering would provide a NIR fluorophore, and contrast those photophysics delineated above for **ArPZnE-TDQ-EArPZn**.

To that end, **Rf_3PZnE-TDQ-ERf_3PZn** and **Rf_3PZnArPPtE-TDQ-EArPPtERf_3PZn** were synthesized by methods closely analogous to those that provided the chromophores discussed above. The steady-state electronic absorption and emission spectra for **Rf_3PZnE-TDQ-ERf_3PZn** reveal features that significantly differ from those of **ArPZnE-TDQ-EArPZn**, while resembling those of **ArPZnE-BTD-EArPZn** (Fig. 5A, Table 1); **Rf_3PZnE-TDQ-ERf_3PZn** spectroscopic highlights include a narrow lowest-energy absorption manifold (Q_x(FWHM) = 1163 cm^{-1}), a modest Stokes shift ($\Delta\nu$ = 851 cm^{-1}), and a substantial fluorescence

 This journal is © The Royal Society of Chemistry 2017

Open Access Article. Published on 07 June 2017. Downloaded on 1/5/2025 1:17:14 AM.
This article is licensed under a Creative Commons Attribution-NonCommercial 3.0 Unported Licence.

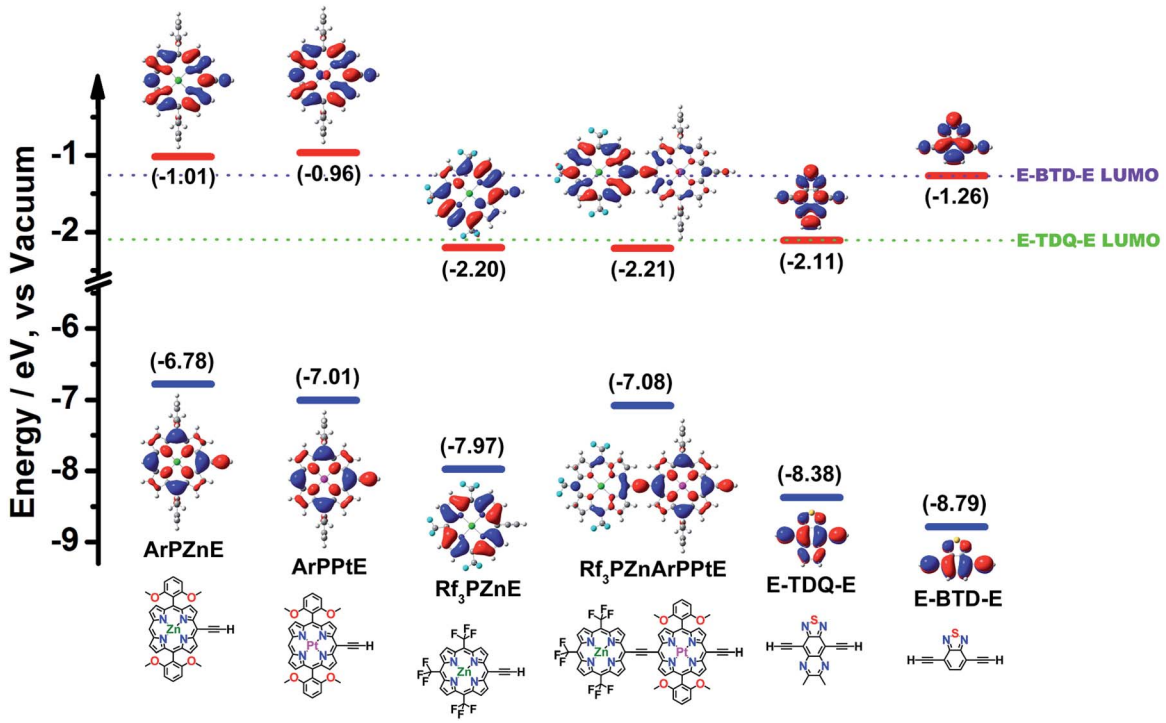

Fig. 4 TD-DFT determined frontier molecular orbitals of the precursor fragments (ArPZnE, ArPPtE, Rf_3PZnE, Rf_3PZnArPPtE, E-TDQ-E, and E-BTD-E) plotted as 0.02 isodensity surfaces along with the corresponding calculated energy levels. Calculations were performed at the M11/6-311g(d) theory level.

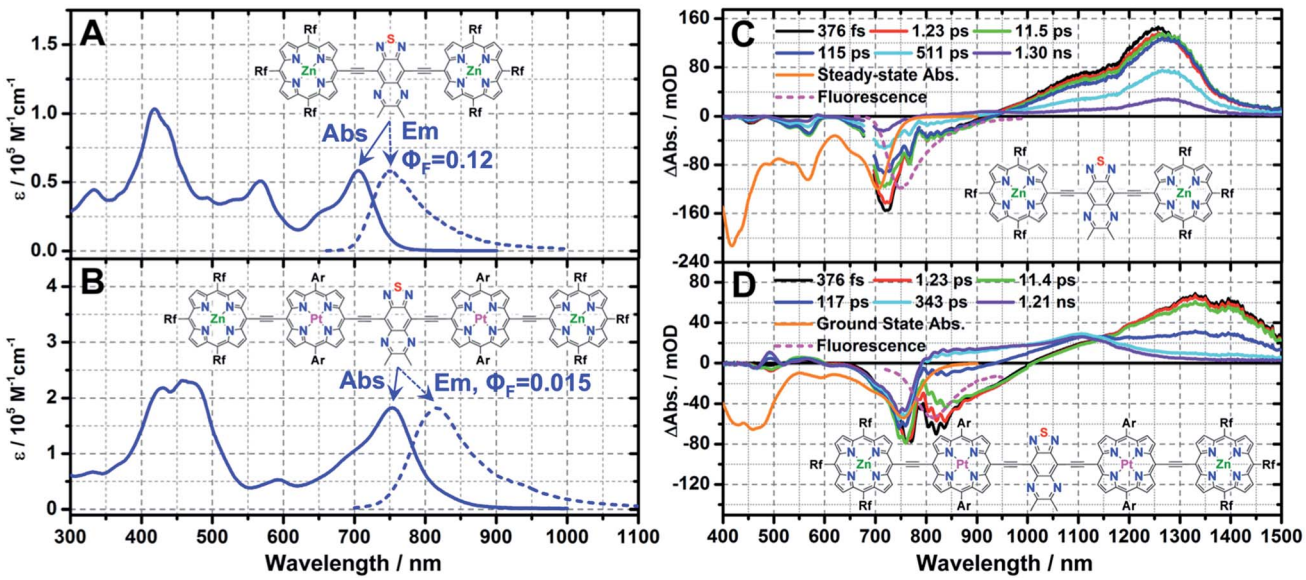

Fig. 5 Steady-state and pump-probe transient absorption spectra recorded for Rf_3PZnE-TDQ-ERf_3PZn and Rf_3PZnArPPtE-TDQ-EArPPtRf_3PZn: steady-state electronic absorption and emission spectra for (A) Rf_3PZnE-TDQ-ERf_3PZn (λ_{exc} = 650 nm for emission) and (B) Rf_3PZnArPPtE-TDQ-EArPPtRf_3PZn (λ_{exc} = 700 nm for emission), solvent = THF, ambient condition. Pump-probe transient absorption spectra recorded at representative time delays for (C) Rf_3PZnE-TDQ-ERf_3PZn (λ_{exc} = 680 nm) and (D) Rf_3PZnArPPtE-TDQ-EArPPtRf_3PZn (λ_{exc} = 800 nm), solvent = THF, ambient temperature, magic angle polarization, steady-state absorption (orange solid line) and fluorescence (magenta dash line) are displayed as inverted spectra. Ar = 2′,6′-bis(3,3-dimethyl-1-butyloxy)phenyl; Rf = heptafluoropropyl.

quantum yield (Φ_F = 0.12) in THF solvent. Likewise, **Rf_3-PZnArPPtE-TDQ-EArPPtRf_3PZn** manifests spectral signatures that reflect attenuated S_1 state CT character relative to the parent chromophore **ArPPtE-TDQ-EArPPt**, and features a low-energy transition having a reduced Q_x(FWHM) (1738 cm^{-1}) and a smaller Stokes shift ($\Delta\nu$ = 945 cm^{-1}) relative to that evinced by

Open Access Article. Published on 07 June 2017. Downloaded on 1/5/2025 1:17:14 AM. This article is licensed under a Creative Commons Attribution-NonCommercial 3.0 Unported Licence.

ArPPtE-TDQ-EArPPt. These steady-state spectroscopic signatures evinced by the *meso*-perfluoroalkyl(porphinato)metal(II) supermolecules vindicate the prediction based on TD-DFT calculations: due to the minimization of ΔE_L, **Rf$_3$PZnE-TDQ-ERf$_3$PZn** and **Rf$_3$PZnArPPtE-TDQ-EArPPtRf$_3$PZn** possess globally delocalized S_1 states having reduced CT character relative to those of **ArPME-TDQ-EArPM**.

Representative transient absorption spectra recorded at selected time delays for **Rf$_3$PZnE-TDQ-ERf$_3$PZn** and **Rf$_3$PZnArPPtE-TDQ-EArPPtRf$_3$PZn** are displayed in Fig. 5C and D; key spectral data are highlighted in Table 2. **Rf$_3$PZnE-TDQ-ERf$_3$PZn** evinces no dynamic Stokes shift in the femtosecond transient absorption spectra, indicating modest CT character of the Franck–Condon state congruent with the minimal ΔE_L calculated for this chromophore. As a result, $S_1 \rightarrow S_0$ internal conversion along the solvation coordinate is greatly diminished, and the S_1 state lifetime of **Rf$_3$PZnE-TDQ-ERf$_3$PZn** reaches ~0.8 ns, comparable to that of **ArPZnE-BTD-EArPZn**. For **Rf$_3$PZnArPPtE-TDQ-EArPPtRf$_3$PZn**, because of the low ΔE_L between the **Rf$_3$PZnArPPtE** wings and the central **TDQ** unit, the $S_0 \rightarrow S_1$ vertical transition involves less electron density redistribution than that of **ArPPtE-TDQ-EArPPt**. As a result, **Rf$_3$PZnArPPtE-TDQ-EArPPtRf$_3$PZn** manifests an ISC rate constant about four times as large as that of the parent chromophore **ArPPtE-TDQ-EArPPt** (6.76×10^{12} s^{-1} *vs.* 1.67×10^{12} s^{-1}), and now displays photophysics that approach those of **ArPPtE-BTD-EArPPt**. Note that these changes of ISC rate constant reflected in the evolution of supermolecular structure from **ArPPtE-TDQ-EArPPt** to **Rf$_3$PZnArPPtE-TDQ-EArPPtRf$_3$PZn** strikingly contrast the corresponding photophysics evinced in classic **PZn$_n$** (Scheme 2) multimeric species, where ISC rate constants decrease dramatically with increasing **PZn$_n$** conjugation length.[8d] The spectroscopic features displayed by **ArPPtE-TDQ-EArPPt** and **Rf$_3$PZnArPPtE-TDQ-EArPPtRf$_3$PZn** highlight the cardinal role of S_1 state proquinoidal character in tuning the NIR ground-state absorption, fluorescence quantum yield, and ISC rate constant for long-wavelength absorbing (porphinato)metal(II) species.

Conclusion

While the influence of proquinoidal character upon the linear absorption spectrum of low optical bandgap π-conjugated polymers and molecules is well understood, less insight exists concerning its impact upon excited-state relaxation pathways and dynamics. Exploiting a series of model highly conjugated NIR-absorbing chromophores based on a (porphinato)metal(II)-spacer-(porphinato)metal(II) (**PM-Sp-PM**) structural motif in which the porphyryl ligand is either electron rich (10,20-diarylporphyrin, **ArP**) or electron deficient (10,15,20-tris(perfluoroalkyl)porphyrin, **Rf$_3$P**), the central metal ion is **Zn(II)** or **Pt(II)**, and the proquinoidal **Sp** is either 4,7-diethynylbenzo[*c*][1,2,5]thiadiazole (**E-BTD-E**) or 4,9-diethynyl-6,7-dimethyl[1,2,5]thiadiazolo[3,4-*g*]quinoxaline (**E-TDQ-E**), we elucidate design principles important for controlling the excited-state dynamics of highly conjugated NIR-absorbing materials that feature conjugation motifs that rely on proquinoidal units, and define strategies through which $S_1 \rightarrow S_0$ radiative (k_r), $S_1 \rightarrow T_1$ intersystem crossing (k_{ISC}), and $S_1 \rightarrow S_0$ internal conversion (k_{IC}) rate constants may be manipulated over many orders of magnitude.

A combination of excited-state dynamical studies and TD-DFT calculations: (i) points to the cardinal role that excited-state configuration interaction (CI) plays in determining the magnitudes of $k_r(S_1 \rightarrow S_0)$, $k_{ISC}(S_1 \rightarrow T_1)$, and $k_{IC}(S_1 \rightarrow S_0)$ in these **PM-Sp-PM** chromophores, and (ii) suggests that a primary determinant of CI magnitude derives from the energetic alignment of the **PM** and **Sp** fragment LUMOs. The chromophore **ArPZnE-BTD-EArPZn**, whose low-lying excited state is characterized by a substantial degree of CI, defines a NIR emitter having a substantial fluorescence quantum yield ($\lambda_{em}(S_1 \rightarrow S_0) = 740$ nm; $\Phi_F = 0.25$); in contrast, **ArPZnE-TDQ-EArPZn**, whose low-lying excited state is described by a modest degree of CI and substantial charge transfer (CT) character, features an internal conversion rate constant, k_{IC}, more than two orders of magnitude larger than its BTD analogue. Optical excitation of **ArPPtE-BTD-EArPPt** likewise generates a low-lying excited state having a substantial extent of CI, and gives rise to unit quantum yield formation of its electronically excited triplet state. In contrast, excitation of **ArPPtE-TDQ-EArPPt** demonstrates an unusually fluorescent **Pt(II)** complex, with an k_{ISC} three orders of magnitude smaller than its **BTD** analogue; the low CI/high CT character of the excited state provides a path to short-circuit the large magnitude spin–orbit coupling associated with heavy metal chromophores by minimizing S_1-state wavefunction density proximal to the heavy **Pt** nuclei, thus realizing a rare if not unique example of a fluorescent (porphinato)platinum(II) chromophore at ambient temperature having ISC dynamics on the ns timescale.[8e,13b,18]

As TD-DFT computations and excited-state dynamical studies correlate high CI with modest energy gaps (ΔE_L) between **PM** and **Sp** fragment LUMOs in **PM-Sp-PM** chromophores, **Rf$_3$PZnE-TDQ-ERf$_3$PZn** and **Rf$_3$PZnArPPtE-TDQ-EArPPtRf$_3$PZn** were synthesized: the σ-electron withdrawing effect of **Rf$_3$PZnE** *meso*-perfluoroalkyl moieties serves to align the **Sp** and **PM** LUMOs of these chromophores, defining NIR absorbers having low-lying excited states characterized by extensive CI. **Rf$_3$PZnE-TDQ-ERf$_3$PZn** thus contrasts **ArPZnE-TDQ-EArPZn** in that NIR fluorescence dominates its photophysics. Likewise, **Rf$_3$PZnArPPtE-TDQ-EArPPtRf$_3$PZn**, because of the low ΔE_L between the **Rf$_3$PZnArPPtE** wings and the central **TDQ** unit, features expansive excited-state CI and a large k_{ISC}, displaying photophysics congruent with large magnitude spin–orbit coupling.

For non-heavy-metal containing low optical bandgap π-conjugated structures that produce long-lived triplet states at high quantum yield, this work shows that these photophysics trace their genesis to the modest degree of CI that characterizes the low-lying excited states of these systems; however, if electronic structural modifications are introduced that give rise to high CI excited states, exceptional fluorophores may be produced. For heavy metal-containing low optical bandgap π-conjugated motifs, this work enables proquinoidal NIR chromophores having counter-intuitive properties to be evolved: for example, while (porphinato)platinum compounds are well

 This journal is © The Royal Society of Chemistry 2017

Open Access Article. Published on 07 June 2017. Downloaded on 1/5/2025 1:17:14 AM. This article is licensed under a Creative Commons Attribution-NonCommercial 3.0 Unported Licence.

known to generate non-emissive triplet states at unit quantum yield upon optical excitation at ambient temperature, diminishing the extent of excited-state CI in these systems realizes long-wavelength absorbing heavy-metal fluorophores. In sum, this work highlights approaches to: (i) modulate low-lying singlet excited-state lifetime over the picosecond-to-nanosecond time domain, (ii) achieve NIR fluorescence with quantum yields up to 25%, (iii) tune the magnitude of the S_1–T_1 ISC rate constant from 10^9 to 10^{12} s^{-1} and (iv) realize T_1-state lifetimes that range from ~0.1 to several μs, for these model **PM-Sp-PM** chromophores, and renders new insights to evolve bespoke photophysical properties for low optical bandgap π-conjugated polymers and molecules based on proquinoidal conjugation motifs.

Given the disparate photophysical requirements for NIR absorbers for applications ranging from optical power limiting to triplet–triplet annihilation photochemistry to *in vivo* bioimaging, this work underscores the photophysical diversity that may be engineered in supermolecular chromophores,[2c,8a,c,d,12,19] and demonstrates how electronic modulation of proquinoidal conjugation motifs, conventionally utilized to regulate the ground-state absorptivity of low optical bandgap π-conjugated polymers and molecules, can also be exploited as powerful means to modulate their excited-state relaxation pathways.

Experimental section

Synthesis and characterization

The synthetic procedures and corresponding characterization data of all new compounds, complete with the reaction schemes, are given in the ESI.†

Instrumentation

Electronic absorption spectra were recorded on a Shimadzu UV-1700 spectrophotometer. Steady-state emission spectra were recorded on a FLS920 spectrometer that utilized a xenon lamp (Xe900) as excitation light source and an extended red sensitive PMT (Hamamatsu R2658P side window photomultiplier, spectral range: 200–1010 nm) or NIR-PMT (Hamamatsu H10330-75, spectral range: 950–1700 nm) for detection. Emission spectra were corrected using a calibration curve supplied with the instrument.

Picosecond fluorescence lifetime measurement system (streak-scope)

Time-resolved emission spectra were recorded using a Hamamatsu C4780 picosecond fluorescence lifetime measurement system. This system employs a Hamamatsu Streakscope C4334 as its photon-counting detector; a Hamamatsu C4792-01 synchronous delay generator electronically generated all time delays. The excitation light source chosen was a Hamamatsu 405 nm diode laser. All fluorescence data were acquired in single-photon-counting mode using Hamamatsu HPD-TA software. The data were analyzed using the Hamamatsu fitting module; both non-deconvoluted and deconvoluted data analyses were performed to ascertain whether or not any emissive processes were excitation pulse-limited.

Femtosecond and nanosecond transient absorption experiments

The transient optical system utilized in this work has been discussed previously.[20] All the samples for pump-probe experiments were deoxygenated *via* three successive freeze–pump–thaw cycles prior to measurement.

Time-dependent density functional theory calculations

All electronic structure calculations were performed upon model compounds in which aliphatic chains were truncated to methyl groups (ESI†). Structure optimization and linear response calculations were performed with density functional theory (DFT) using Gaussian 09, revision C.1.[21] The M11 (ref. 22) functional was employed for all calculations. Optimizations were performed with minimal symmetry constraints using tight optimization criteria; initial optimizations used smaller basis sets but the final optimizations and TD-DFT calculations employed the 6-311g(d) basis set[23] as implemented in Gaussian 09. Selected frontier orbital wave functions were plotted as isosurfaces (iso = 0.02) using Gaussview 5.[24] TD-DFT result files were post-processed using the GaussSum package;[25] this software partitions the wave function amplitudes onto atomic components using Mulliken population analysis,[26] and parses the electronic configurations contributing to each excitation.

Conflict of interest

No competing financial interests have been declared.

Acknowledgements

This work was funded by the Division of Chemical Sciences, Geosciences, and Biosciences, Office of Basic Energy Sciences, of the U.S. Department of Energy through Grant DE-SC0001517. J. L., P. Z., and D. N. B. acknowledge financial support from the National Institutes of Health through Grant GM048043.

References

1 (*a*) L. Dou, Y. Liu, Z. Hong, G. Li and Y. Yang, *Chem. Rev.*, 2015, **115**, 12633–12665; (*b*) Y. Zhao, Y. Guo and Y. Liu, *Adv. Mater.*, 2013, **25**, 5372–5391; (*c*) G. Li, R. Zhu and Y. Yang, *Nat. Photonics*, 2012, **6**, 153–161; (*d*) C. W. Spangler, *J. Mater. Chem.*, 1999, **9**, 2013–2020; (*e*) J. V. Frangioni, *Curr. Opin. Chem. Biol.*, 2003, **7**, 626–634.

2 (*a*) T. D. Lash, P. Chandrasekar, A. T. Osuma, S. T. Chaney and J. D. Spence, *J. Org. Chem.*, 1998, **63**, 8455–8469; (*b*) J. J. Piet, P. N. Taylor, H. L. Anderson, A. Osuka and J. M. Warman, *J. Am. Chem. Soc.*, 2000, **122**, 1749–1757; (*c*) K. Susumu, T. V. Duncan and M. J. Therien, *J. Am. Chem. Soc.*, 2005, **127**, 5186–5195; (*d*) C.-Y. Lin, Y.-C. Wang, S.-J. Hsu, C.-F. Lo and E. W.-G. Diau, *J. Phys. Chem. C*, 2010, **114**, 687–693; (*e*) H. J. Song, D. H. Kim, T. H. Lee and

Open Access Article. Published on 07 June 2017. Downloaded on 1/5/2025 1:17:14 AM.
This article is licensed under a Creative Commons Attribution-NonCommercial 3.0 Unported Licence.

D. K. Moon, *Eur. Polym. J.*, 2012, **48**, 1485–1494; (*f*) Y. Huang, L. Li, X. Peng, J. Peng and Y. Cao, *J. Mater. Chem.*, 2012, **22**, 21841–21844; (*g*) S. Mathew, A. Yella, P. Gao, R. Humphry-Baker, B. F. E. Curchod, N. Ashari-Astani, I. Tavernelli, U. Rothlisberger, M. K. Nazeeruddin and M. Grätzel, *Nat. Chem.*, 2014, **6**, 242–247; (*h*) M. Morisue, Y. Hoshino, M. Nakamura, T. Yumura, S. Machida, Y. Ooyama, M. Shimizu and J. Ohshita, *Inorg. Chem.*, 2016, **55**, 7432–7441; (*i*) N. Jiang, G. Zuber, S. Keinan, A. Nayak, W. Yang, M. J. Therien and D. N. Beratan, *J. Phys. Chem. C*, 2012, **116**, 9724–9733; (*j*) K. Susumu and M. J. Therien, *J. Porphyrins Phthalocyanines*, 2015, **19**, 205–218.

3 M. Urbani, M. Grätzel, M. K. Nazeeruddin and T. Torres, *Chem. Rev.*, 2014, **114**, 12330–12396.

4 (*a*) G.-J. Zhou and W.-Y. Wong, *Chem. Soc. Rev.*, 2011, **40**, 2541–2566; (*b*) M. Calvete, G. Y. Yang and M. Hanack, *Synth. Met.*, 2004, **141**, 231–243.

5 (*a*) T. N. Singh-Rachford and F. N. Castellano, *Coord. Chem. Rev.*, 2010, **254**, 2560–2573; (*b*) J. Zhao, S. Ji and H. Guo, *RSC Adv.*, 2011, **1**, 937–950; (*c*) J. Zhao, W. Wu, J. Sun and S. Guo, *Chem. Soc. Rev.*, 2013, **42**, 5323–5351.

6 (*a*) S. A. Hilderbrand and R. Weissleder, *Curr. Opin. Chem. Biol.*, 2010, **14**, 71–79; (*b*) L. Yuan, W. Lin, K. Zheng, L. He and W. Huang, *Chem. Soc. Rev.*, 2013, **42**, 622–661; (*c*) P. P. Ghoroghchian, M. J. Therien and D. A. Hammer, *Wiley Interdiscip. Rev.: Nanomed. Nanobiotechnol.*, 2009, **1**, 156–167.

7 (*a*) S. Takahashi, Y. Kuroyama, K. Sonogashira and N. Hagihara, *Synthesis*, 1980, 627–630; (*b*) S. G. DiMagno, V. S.-Y. Lin and M. J. Therien, *J. Org. Chem.*, 1993, **58**, 5983–5993; (*c*) S. G. DiMagno, V. S.-Y. Lin and M. J. Therien, *J. Am. Chem. Soc.*, 1993, **115**, 2513–2515; (*d*) S. M. LeCours, H.-W. Guan, S. G. DiMagno, C. H. Wang and M. J. Therien, *J. Am. Chem. Soc.*, 1996, **118**, 1497–1503.

8 (*a*) V. S.-Y. Lin, S. G. DiMagno and M. J. Therien, *Science*, 1994, **264**, 1105–1111; (*b*) V. S.-Y. Lin and M. J. Therien, *Chem.–Eur. J.*, 1995, **1**, 645–651; (*c*) K. Susumu and M. J. Therien, *J. Am. Chem. Soc.*, 2002, **124**, 8550–8552; (*d*) T. V. Duncan, K. Susumu, L. E. Sinks and M. J. Therien, *J. Am. Chem. Soc.*, 2006, **128**, 9000–9001; (*e*) T. V. Duncan, P. R. Frail, I. R. Miloradovic and M. J. Therien, *J. Phys. Chem. B*, 2010, **114**, 14696–14702.

9 (*a*) R. Kumble, S. Palese, V. S.-Y. Lin, M. J. Therien and R. M. Hochstrasser, *J. Am. Chem. Soc.*, 1998, **120**, 11489–11498; (*b*) R. Shediac, M. H. B. Gray, H. T. Uyeda, R. C. Johnson, J. T. Hupp, P. J. Angiolillo and M. J. Therien, *J. Am. Chem. Soc.*, 2000, **122**, 7017–7033; (*c*) I. V. Rubtsov, K. Susumu, G. I. Rubtsov and M. J. Therien, *J. Am. Chem. Soc.*, 2003, **125**, 2687–2696.

10 (*a*) N. J. Turro, V. Ramamurthy and J. C. Scaiano, *Modern Molecular Photochemistry of Organic Molecules*, University Science Books, Sausalito, Calif., 2010; (*b*) Z. R. Grabowski, K. Rotkiewicz and W. Rettig, *Chem. Rev.*, 2003, **103**, 3899–4031; (*c*) P. Panda, D. Veldman, J. Sweelssen, J. J. A. M. Bastiaansen, B. M. W. Langeveld-Voss and S. C. J. Meskers, *J. Phys. Chem. B*, 2007, **111**, 5076–5081.

11 (*a*) D. Eastwood and M. Gouterman, *J. Mol. Spectrosc.*, 1970, **35**, 359–375; (*b*) M. Gouterman, *Optical Spectra and Electronic Structure of Porphyrins*, Academic Press, New York, 1978; (*c*) A. Harriman, *J. Chem. Soc., Faraday Trans. 2*, 1981, **77**, 1281–1291.

12 T. V. Duncan, T. Ishizuka and M. J. Therien, *J. Am. Chem. Soc.*, 2007, **129**, 9691–9703.

13 (*a*) R. S. Becker and J. B. Allison, *J. Phys. Chem.*, 1963, **67**, 2662–2669; (*b*) J. R. Sommer, A. H. Shelton, A. Parthasarathy, I. Ghiviriga, J. R. Reynolds and K. S. Schanze, *Chem. Mater.*, 2011, **23**, 5296–5304.

14 (*a*) A. Samanta, *J. Phys. Chem. B*, 2006, **110**, 13704–13716; (*b*) M. Glasbeek and H. Zhang, *Chem. Rev.*, 2004, **104**, 1929–1954.

15 I. V. Khudyakov, Y. A. Serebrennikov and N. J. Turro, *Chem. Rev.*, 1993, **93**, 537–570.

16 (*a*) S. G. DiMagno, R. A. Williams and M. J. Therien, *J. Org. Chem.*, 1994, **59**, 6943–6948; (*b*) J. G. Goll, K. T. Moore, A. Ghosh and M. J. Therien, *J. Am. Chem. Soc.*, 1996, **118**, 8344–8354; (*c*) J. Rawson, A. C. Stuart, W. You and M. J. Therien, *J. Am. Chem. Soc.*, 2014, **136**, 17561–17569.

17 J. Rawson, Exploration of Porphyrin-based Semiconductors for Negative Charge Transport, Ph.D. thesis, Duke University, Durham, NC, 2014.

18 (*a*) A. Vogler, H. Kunkely and B. Rethwisch, *Inorg. Chim. Acta*, 1980, **46**, 101–105; (*b*) T. Kobayashi, K. D. Straub and P. M. Rentzepis, *Photochem. Photobiol.*, 1979, **29**, 925–931; (*c*) K. D. Straub, P. M. Rentzepis and D. Huppert, *J. Photochem.*, 1981, **17**, 419–425.

19 T. V. Duncan, I. V. Rubtsov, H. T. Uyeda and M. J. Therien, *J. Am. Chem. Soc.*, 2004, **126**, 9474–9475.

20 J. Park, P. Deria and M. J. Therien, *J. Am. Chem. Soc.*, 2011, **133**, 17156–17159.

21 M. J. Frisch, G. W. Trucks, H. B. Schlegel, G. E. Scuseria, M. A. Robb, J. R. Cheeseman, G. Scalmani, V. Barone, B. Mennucci, G. A. Petersson, H. Nakatsuji, M. Caricato, X. Li, H. P. Hratchian, A. F. Izmaylov, J. Bloino, G. Zheng, J. L. Sonnenberg, M. E. Hada, M. K. Toyota, R. Fukuda, J. Hasegawa, M. Ishida, T. Nakajima, Y. Honda, O. Kitao, H. Nakai, T. Vreven, J. A. Montgomery, J. E. Peralta, F. Ogliaro, M. Bearpark, J. J. Heyd, E. Brothers, K. N. Kudin, V. N. Staroverov, R. Kobayashi, J. Normand, K. Raghavachari, A. Rendell, J. C. Burant, S. S. Iyengar, J. Tomasi, M. Cossi, N. Rega, J. M. Millam, M. Klene, J. E. Knox, J. B. Cross, V. Bakken, C. Adamo, J. Jaramillo, R. Gomperts, R. E. Stratmann, O. Yazyev, A. J. Austin, R. Cammi, C. Pomelli, J. W. Ochterski, R. L. Martin, K. Morokuma, V. G. Zakrzewski, G. A. Voth, P. Salvador, J. J. Dannenberg, S. Dapprich, A. D. Daniels, Ö. Farkas, J. B. Foresman, J. V. Ortiz, J. Cioslowski and D. J. Fox, *Rev. C.1.*, Gaussian, Inc., Wallingford CT, 2009.

22 R. Peverati and D. G. Truhlar, *J. Phys. Chem. Lett.*, 2011, **2**, 2810–2817.

23 (*a*) A. J. H. Wachters, *J. Chem. Phys.*, 1970, **52**, 1033–1036; (*b*) P. J. Hay, *J. Chem. Phys.*, 1977, **66**, 4377–4384; (*c*) R. Krishnan, J. S. Binkley, R. Seeger and J. A. Pople, *J. Chem. Phys.*, 1980, **72**, 650–654; (*d*) A. D. McLean and G. S. Chandler, *J. Chem.*

 This journal is © The Royal Society of Chemistry 2017

Open Access Article. Published on 07 June 2017. Downloaded on 1/5/2025 1:17:14 AM.
This article is licensed under a Creative Commons Attribution-NonCommercial 3.0 Unported Licence.

Phys., 1980, **72**, 5639–5648; (*e*) K. Raghavachari and G. W. Trucks, *J. Chem. Phys.*, 1989, **91**, 1062–1065; (*f*) R. C. Binning and L. A. Curtiss, *J. Comput. Chem.*, 1990, **11**, 1206–1216; (*g*) M. P. McGrath and L. Radom, *J. Chem. Phys.*, 1991, **94**, 511–516; (*h*) L. A. Curtiss, M. P. McGrath, J.-P. Blaudeau, N. E. Davis, R. C. Binning and L. Radom, *J. Chem. Phys.*, 1995, **103**, 6104–6113; (*i*) J.-P. Blaudeau, M. P. McGrath, L. A. Curtiss and L. Radom, *J. Chem. Phys.*, 1997, **107**, 5016–5021.

24 R. Dennington, T. Keith and J. Millam, *GaussView Ver. 5, Semichem Inc.*, Shawnee Mission, KS, 2009.

25 N. M. O'Boyle, A. L. Tenderholt and K. M. Langner, *J. Comput. Chem.*, 2008, **29**, 839–845.

26 R. S. Mulliken, *J. Chem. Phys.*, 1955, **23**, 1833–1840.